This is the peer reviewd version of the followng article:

Sound velocities and single-crystal elasticity of hydrous Fo90 olivine to 12 GPa / Faccincani, L., Criniti, G., Kurnosov, A., Ballaran, T.B., Withers, A.C., Mazzucchelli, M., Nestola, F., Coltorti, M.. - In: PHYSICS OF THE EARTH AND PLANETARY INTERIORS. - ISSN 0031-9201. - 337:(2023), pp. 1-13. [10.1016/j.pepi.2023.107011]

Terms of use:

The terms and conditions for the reuse of this version of the manuscript are specified in the publishing policy. For all terms of use and more information see the publisher's website.

15/11/2026 15:46

(Article begins on next page)

Sound velocities and single-crystal elasticity of hydrous Fo90 olivine to 12 GPa

Luca Faccincani [1,2,*], Giacomo Criniti [3], Alexander Kurnosov [3], Tiziana Boffa Ballaran [3], Anthony C. Withers [3], Maurizio Mazzucchelli [4], Fabrizio Nestola [5] and Massimo Coltorti [1,2,6]

[1] *Department of Physics and Earth Sciences, University of Ferrara, Via Saragat 1, 44122 Ferrara, Italy*

[2] *Department of Environmental and Prevention Sciences, University of Ferrara, C.so Ercole I D'Este 32, 44121 Ferrara, Italy*

[3] *Bayerisches Geoinstitut, University of Bayreuth, Universitätsstraße 30, 95440 Bayreuth, Germany*

[4] *Department of Chemical and Geological Sciences, University of Modena and Reggio Emilia, Via Campi 103, 41125 Modena, Italy*

[5] *Department of Geosciences, University of Padua, Via Gradenigo 6, 35131 Padua, Italy*

[6] *Istituto Nazionale di Geofisica e Vulcanologia (INGV) Sezione di Palermo, Via Ugo la Malfa 153, 90146 Palermo, Italy*

*** Corresponding author:** Luca Faccincani; email: luca.faccincani@unife.it

Abstract

Nominally anhydrous minerals (NAMs) may contain significant amounts of water and constitute an important reservoir for mantle hydrogen. The colloquial term 'water' in NAMs is related to the presence of hydroxyl-bearing (OH^-) point defects in their crystal structure, where hydrogen is bonded to lattice oxygen and is charge-balanced by cation vacancies. This hydrous component may therefore have substantial effects on the thermoelastic parameters of NAMs, comparable to other major crystal-chemical substitutions (e.g., Fe, Al). Assessment of water concentrations in natural minerals from mantle xenoliths indicates that olivine commonly stores ~0 – 200 ppm of water. However, the lack of samples originating from depths exceeding ~250 km coupled with the rapid diffusion of hydrogen

in olivine at magmatic temperatures makes the determination of the olivine water content in the upper mantle challenging. On the other hand, numerous experimental data show that, at pressures and temperatures corresponding to deep upper mantle conditions, the water storage capacity of olivine increases to 0.2 – 0.5 wt.%. Therefore, determining the elastic properties of olivine samples with more realistic water contents for deep upper mantle conditions may help in interpreting both seismic velocity anomalies in potentially hydrous regions of Earth's mantle as well as the observed seismic velocity and density contrasts across the 410-km discontinuity.

Here, we report simultaneous single-crystal X-ray diffraction and Brillouin scattering experiments at room temperature up to 11.96(2) GPa on hydrous (0.20(3) wt.% H_2O) Fo90 olivine to assess its full elastic tensor, and complement these results with a careful re-analysis of all the available single-crystal elasticity data from the literature for anhydrous Fo90 olivine. While the bulk (K) and shear (G) moduli of hydrous Fo90 olivine are virtually identical to those of the corresponding anhydrous phase, their pressure derivatives K' and G' are slightly larger, although consistent within mutual uncertainties. We then defined linear relations between the water concentration in Fo90 olivine, the elastic moduli and their pressure derivatives, which were then used to compute the sound velocities of Fo90 olivine with higher degrees of hydration. Even for water concentrations as high as 0.5 wt.%, the sound wave velocities of hydrous and anhydrous olivines were found to be identical within uncertainties at pressures corresponding to the base of the upper mantle. Contrary to previous claims, our data suggest that water in olivine is not seismically detectable, at least for contents consistent with deep upper mantle conditions. In addition to that, our data reveal that the hydration of olivine is unlikely to be a key factor in reconciling seismic velocity and density contrasts across the 410-km discontinuity with a pyrolitic mantle.

Keywords: hydrous olivine, Brillouin scattering, elasticity, high pressure; NAMs

1. Introduction

Although commonly referred to as nominally anhydrous minerals (NAMs), the dominant phases of Earth's upper mantle may contain significant amounts of water (e.g., Bell and Rossman, 1992). The occurrence of water in NAMs is closely related to the presence of hydrogen in their crystal structures, which is bonded to oxygen atoms forming hydroxyl-bearing (OH^-) point defects and its incorporation is typically charge-balanced by the formation of cation vacancies. Olivine, α-$(Mg,Fe)_2SiO_4$, is considered to be the most abundant mineral of Earth's upper mantle and to constitute about 60 vol.% of pyrolitic phase assemblages (Ringwood, 1975). The water concentration detected in natural olivine samples from mantle xenoliths is generally low, in the order of 0 – 200 ppm wt. (Beran and Libowitzky, 2006; Novella et al., 2015; Peslier et al., 2010). Although a growing body of water analyses of olivine is available in the literature (Bonadiman et al., 2009; Peslier, 2010; Xia et al., 2010, etc.), trends between water content and its distribution across different geological settings are still difficult to determine, as well as the actual abundance of water in olivine in the upper mantle. This is due to both the rapid diffusion of hydrogen in olivine at magmatic temperatures (e.g., Demouchy and Mackwell, 2006), which leads to partial dehydration of olivine in mantle xenoliths during their ascent, and the lack of xenoliths originating from depths greater than ~250 km. Even though the fast ascent of kimberlite magmas should prevent dehydration in olivine during xenolith transport (Demouchy et al., 2006; Peslier et al., 2008), in contrast to olivines from xenoliths found in alkali basalts which are commonly affected by H loss (e.g., Peslier et al., 2008), our understanding of how the water content of olivines changes as a function of depth largely relies on experimental studies. Indeed, a plethora of experimental data on water solubility in olivines at pressures and temperatures relevant to the upper mantle are available and indicate much higher water contents compared to those detected in natural olivine samples, especially at deep upper mantle conditions where the water storage capacity of olivine increases to 0.2 – 0.5 wt.% (e.g., Férot and Bolfan-Casanova, 2012; Hirschmann et al., 2005; Mosenfelder, 2006). Therefore, synthetic olivine samples with a more realistic water content expected for deep upper mantle conditions warrant investigation,

as this may improve our understanding of various geodynamic processes operating on Earth (Regenauer-Lieb, 2006).

Water incorporation in olivine, even in trace amounts, has long been known to have substantial effects on its physical and chemical properties, such as atomic diffusivity, electrical conductivity, thermal conductivity, rheology, and melting (e.g., Chang et al., 2017; Costa and Chakraborty, 2008; Inoue, 1994; Jung and Karato, 2001; Smyth et al., 2006). From a crystal-chemical perspective, hydrogen incorporation in the crystal structure of olivine may occur both in the octahedral M sites, $Mg^{2+} \leftrightarrow 2H^{+}$, and in tetrahedral T sites, $Si^{4+} \leftrightarrow 4H^{+}$ (e.g., Brodholt and Refson, 2000; Hushur et al., 2009; Smyth et al., 2006). Previous experimental studies about the substitution mechanism of water in olivine showed contrasting results, although it was recognized that the synthesis conditions (pressure and SiO_2 activity) were influencing factors (e.g., Bali et al., 2008; Férot and Bolfan-Casanova, 2012; Matveev et al., 2001; Withers and Hirschmann, 2008). However, recent electron microprobe (EPMA) data coupled with transmission Fourier transform infrared spectroscopy (FTIR) analyses (Fei and Katsura, 2020), solid-state nuclear magnetic resonance (NMR) spectroscopy (Xue et al., 2017), and first-principles calculations studies (Umemoto et al., 2011; Xue et al., 2017) suggest that hydrogen substitution in olivine mainly occurs at the T sites at high pressure. Therefore, hydrogen incorporation in the M sites can be ruled out from being the predominant substitution mechanism in olivine under typical mantle conditions, as its occurrence is restricted to shallow depths ($\leq$ 80 km) and high SiO_2 activity (Bali et al., 2008; Fei and Katsura, 2020; Withers et al., 2011).

Despite its possible geophysical relevance, the effect of water on the elastic properties of olivine has been poorly constrained. The only elasticity measurements available in the literature were conducted by Mao et al. (2010) on hydrous (0.89 wt.% H_2O) end-member forsterite (Fo100) single crystals up to 14 GPa and by Jacobsen et al. (2008, 2009) on hydrous (0.8 wt.% H_2O) Fo97 olivine single crystals at ambient pressure. These works showed that the incorporation of water into pure forsterite and near end-member compositions is accompanied by a considerable reduction of the bulk (K_S) and shear (G) moduli at ambient conditions. However, owing to the much larger moduli pressure

derivatives of the hydrated samples, K_S and G of the hydrous Fo100 at high pressure are greater than those of the corresponding anhydrous phase (Mao et al., 2010). Nonetheless, the effect of hydration on the elasticity of the more relevant Fo90 olivine mantle composition remains largely unconstrained because no experimental data are available. Furthermore, previous works studied hydrous samples containing 0.8-0.9 wt.% H_2O, which is well above the expected water content for olivine at deep upper mantle conditions (e.g., Férot and Bolfan-Casanova, 2012; Hirschmann et al., 2005; Mosenfelder, 2006).

In this work, we set out to investigate the effect of hydration on the elastic properties of hydrous Fo90 olivine samples with more realistic water content for deep upper mantle conditions, as it may help in interpreting both seismic velocity anomalies in potentially hydrous regions of Earth's mantle as well as the observed seismic velocity and density contrasts across the 410-km discontinuity. To this aim, we performed simultaneous single-crystal X-ray diffraction (SCXRD) and Brillouin scattering measurements at room temperature up to 11.96(2) GPa on hydrous (0.20(3) wt.% H_2O) Fo90 olivine to constrain its full elastic tensor. By comparing our new accurate data with those available from literature for anhydrous Fo90 olivine, we evaluated the combined effect of H_2O and Fe incorporation on the pressure-dependent elasticity of olivine. Our measurements are suitable to determine the sound wave velocities of hydrous Fo90 olivine at pressures corresponding to the base of the upper mantle, to be integrated in theoretical/experimental studies attempting to constrain the olivine abundance and water content at the 410-km discontinuity.

2. Materials and Methods

Large (200 – 500 μm) and homogeneous single crystals of hydrous Fo90 olivine used in this study were previously synthesized and characterized by Withers et al. (2011, 2012, sample M475). Major element concentrations determined by wavelength-dispersive EPMA analysis indicate the Mg# of synthesized olivines to be 90.2(1), and water content was determined to be ~0.20(3) wt.% based on elastic recoil detection analysis (ERDA) (Withers et al., 2012). Polarized FTIR spectroscopy and

secondary ion mass spectroscopy (SIMS) measurements were also conducted on the same sample, showing excellent agreement with one another (Withers et al., 2012).

High-pressure Brillouin scattering measurements in DAC are conducted in the so-called platelet geometry (Speziale et al., 2014; Whitfield et al., 1976). For olivine, at least two crystal platelets with different crystallographic orientations are required to obtain the nine independent elastic stiffness coefficients (c_{ij}) given its orthorhombic symmetry. The full elastic tensor is obtained by a least-square fit of experimentally determined densities and sound wave velocities measured in different crystallographic directions using the Christoffel's equation:

$$\left|c_{ijkl}q_j q_l - \rho v_i^2 \delta_{ik}\right| = 0 \quad (1)$$

where c_{ijkl} are the elastic stiffness coefficients in tensorial notation (e.g., Nye, 1985), q_j and q_l are direction cosines, ρ is the density, v_i are the sound wave velocities and δ_{ik} is the Kronecker delta. To obtain accurate and precise c_{ij} values, it is important that their correlation in the fit procedure is low. This is achieved by using two appropriate crystallographic orientations (Criniti et al., 2021). We used published c_{ij} data for Fo90 olivine (Abramson et al., 1997) to simulate the shear (v_S) and compressional velocities (v_P) for different crystallographic planes. Synthetic v_S and v_P were randomly scattered by up to ± 30 or ± 60 m/s, respectively, to simulate realistic datasets and to obtain realistic uncertainties in the inversion procedure. Platelets with direction cosines (0.32, 0.91, 0.26) and (0.78, 0.02, 0.62), corresponding to 101 and 161 *hkl* indices, were chosen for high-pressure measurements.

Hydrous Fo90 olivine single crystals were first observed under a polarising microscope and selected based on the absence of inclusions and their sharp optical extinction. Preliminary X-ray diffraction measurements were carried out on a Huber single-crystal diffractometer equipped with a point detector and Mo$K\alpha$ radiation, and driven by the software SINGLE (Angel and Finger, 2011). Sharp diffraction peaks (full width half maxima < 0.055°) were observed upon omega-scan rotations for each crystal, confirming that they are of high quality. Two crystals were selected and subsequently oriented parallel to the (101) or (161) crystallographic plane, glued on a glass slide and polished on both sides to obtain platelets (crystals X1 and X2, respectively) with a thickness of ~15 μm. The two

platelets were then cut into semi-circular or rectangular shapes (Figure 1) using a FEI Scios focused ion beam (Schulze et al., 2017), operated at 30 nA and 30 kV.

High-pressure SCXRD and Brillouin scattering measurements were carried out in a BX-90 piston-cylinder-type diamond anvil cell (DAC) (Kantor et al., 2012) equipped with Almax-Boehler diamond anvils having culets of 500 μm in diameter and conical seats with large opening angles (Boehler and De Hantsetters, 2004). A Re gasket was indented to a thickness of ~ 70 μm and drilled with an infrared laser to obtain the sample chamber. The two FIB-cut crystal platelets were loaded into the same sample chamber together with a ruby sphere (Figure 1) for pressure determination following the calibration reported by Shen et al. (2020). Pre-compressed helium was loaded as quasi-hydrostatic pressure transmitting medium using the gas loading apparatus installed at the Bayerisches Geoinstitut, University of Bayreuth (Kurnosov et al., 2008).

High-pressure SCXRD and Brillouin scattering measurements were conducted using the system installed at the Bayerisches Geoinstitut, University of Bayreuth (Trots et al., 2011, 2013). The Brillouin scattering system consists of a Coherent Verdi V2 solid-state Nd:YVO_4 laser with a 532 nm single wavelength output and a six-pass Sandercock-type tandem Fabry-Perot interferometer (Sandercock, 1982) equipped with a Hamamatsu C11202-50 detector. A source laser power of 100 or 150 mW was used for room pressure and high-pressure measurements, respectively. All measurements were performed in platelet geometry with an external scattering angle of 79.5°, which was calibrated using a fused silica glass standard. Periodic measurements of the standard revealed deviations within ±0.1º, which correspond to shifts of up to ±0.1% in the calculated velocities, well within our experimental uncertainty. Dispersion curves of sound wave velocities versus crystallographic orientation were collected by rotation of the χ circle of the diffractometer between -170° and 180° at steps of 10° or 20°. Densities were derived at each pressure from single-crystal diffraction measurements, which were performed on the same goniometer using a Huber Eulerian single-crystal X-ray diffractometer equipped with a point detector. The system is coupled with an ultra-high intensity rotating anode X-ray source (Mo$K\alpha$, FR-E^+ SuperBright from Rigaku) operated

179 at 55 kV and 45 mA and multilayer VaryMax^{TM} focusing optics, and was driven by the software
180 SINGLE (Angel and Finger, 2011). At each pressure point, 14-18 Bragg reflections for each crystal
181 were centred using the eight position centring method (King and Finger, 1979), and cell parameters
182 were determined by vector least-square refinement (Ralph and Finger, 1982).

183 # 3. Results and discussion

184 ## 3.1 Compressibility of hydrous Fo90 olivine

185 High-pressure SCXRD measurements were conducted at seven pressure points, ranging from
186 ambient pressure to ~12 GPa. Unit-cell lattice parameters and volumes of both hydrous Fo90 olivine
187 single crystals investigated in this study are reported in Table 1. The two crystals have slightly
188 different volumes, V (X1) > V (X2), with crystal X1 showing larger uncertainties on the measured
189 lattice parameters. This is due to its crystallographic orientation, which limits the observations in both
190 a* and c*. Therefore, lattice parameters measured for crystal X2 are likely more accurate. The
191 variation with pressure of the lattice parameters and volumes, normalized with respect to their room
192 pressure values, are reported in Figure 2 and compared with literature data. Hydrous olivine is most
193 compressible along the **b**-direction ([010]) and least compressible along the **a**-direction ([100]), as
194 also observed for end-member Fo100 and Fo90 (e.g., Downs et al., 1996; Pamato et al., 2019). The
195 EoSFit7c program was used to fit the *P*-*V* data of both crystals using a third-order Birch-Murnaghan
196 Equation of State (BM3 EoS) (Angel et al., 2014):

197 $$P = \frac{3}{2}K_{T0}\left[\left(\frac{V_0}{V}\right)^{\frac{7}{3}} - \left(\frac{V_0}{V}\right)^{\frac{5}{3}}\right]\left\{1 + \frac{3}{4}(K'_{T0} - 4)\left[\left(\frac{V_0}{V}\right)^{\frac{2}{3}} - 1\right]\right\} \quad (2)$$

198 where V_0 is the ambient pressure unit-cell volume, K_{T0} the isothermal bulk modulus and K'_{T0} its
199 pressure derivative. The resulting BM-EoS parameters, simultaneously refined using the data
200 weighted by the uncertainties in P and V, are: V_0 = 291.65(2) Å^3, K_{T0} = 124.5(1.0) GPa and K' =
201 4.5(2), where values in parenthesis correspond to 1σ uncertainties on each parameter. The fitted V_0
202 value is in excellent agreement (within 1σ) with the unit-cell volume measured at room pressure for
203 crystal X2. To judge the correctness of truncation of the BM-EoS to third order and to assess whether

204 higher order terms (K'') might be significant in the EoS, we plotted the Eulerian finite strain (f_E)
205 versus the normalized stress (F_E) (f_E-F_E plot; Angel, 2000) (Supplementary Figure S1). Assessment
206 of the f_E-F_E plot indicates that data are adequately described by a BM-EoS truncated to third order.
207 Moreover, we have constructed confidence ellipses (Angel, 2000) in K_{T0} and K'_{T0} obtained for the fit
208 to the hydrous olivine *P*-*V* dataset to visualise the extent of the correlation between such parameters
209 and to assess the quality of the EoS (Supplementary Figure S1). Following the approach of Angel
210 (2000) and Angel et al. (2014), linearized BM3 EoSs have been used to fit the variation with pressure
211 of the a-, b- and c-axis by substituting V with l^3, $3K_{T0}$ with $M_{l,0}$ and $3K'_{T0}$ with $M'_{l,0}$:

212 $$P = \frac{1}{2}M_{l,0}\left[\left(\frac{l_0}{l}\right)^7 - \left(\frac{l_0}{l}\right)^5\right]\left\{1 + \frac{1}{4}\left(M'_{l,0} - 12\right)\left[\left(\frac{l_0}{l}\right)^2 - 1\right]\right\} \quad (3)$$

213 The resulting EoS parameters are: a_0 = 4.7610(1) Å, M_{0a} = 539.1(5.7) GPa, M'_a= 23.7(1.4), b_0 =
214 10.2238(3) Å, M_{0b} = 283.4(2.8) GPa, M'_b= 10.7(6) and c_0 = 5.9921(1) Å, M_{0c} = 372.1(2.6) GPa, M'_c=
215 12.1(5). As described in Angel et al. (2014), the linear moduli and their pressure derivatives defined
216 in this fashion have numerical values three times those of the corresponding K_{T0} and, therefore, must
217 be divided by three in order to return volume-like values. The resulting axial compressibility for the
218 hydrous olivine follows the scheme $\beta_b > \beta_c > \beta_a$ (as observed for the anhydrous phase) and the
219 obtained $M_{l,0}$ and $M'_{l,0}$ values compare well with those of the anhydrous phase reported in the
220 literature, as discussed later.

221 Angel et al. (2018) recently reviewed all the published single-crystal data that constrain the elastic
222 properties and EoS of mantle-composition olivine (Fo90 to Fo92), also testing the mutual consistency
223 of the different datasets used. Therefore, data selected by Angel et al. (2018) will be used as a
224 comparison for hydrous olivine. The unit-cell lattice parameters reported by Nestola et al. (2011) and
225 Zha et al. (1998), normalized to their corresponding room pressure values, are compared to the single
226 crystal hydrous Fo90 olivine data obtained in this study (Figure 2). When compared to the *P*-*V* and
227 linearized BM3 EoS fits of the hydrous Fo90 olivine data obtained in this study, the relative
228 compression curves (lattice parameters and volumes) for the corresponding anhydrous phase show

good agreement. Hence, we do not observe anomalies in the axial compressibility scheme or the unit-cell volume compression of the hydrous phase.

3.2 Sound wave velocities of hydrous Fo90 olivine and c_{ij} inversion strategy

Sound wave velocities of hydrous Fo90 olivine were measured at seven pressure points, ranging from ambient pressure to ~12 GPa, i.e., the same conditions of SCXRD measurements (Table 2). Typical Brillouin spectra collected in the low- and high-pressure range (Figure 3a) show distinct and resolved compressional v_P and shear (v_{S1} and v_{S2}) wave velocities peaks for most ranges of rotation angle (χ) (Figure 3b). To obtain the nine elastic stiffness coefficients c_{ij}, the Christoffel's equation (Equation 1) is usually solved using a non-linear least-squares inversion of the density and all the acoustic velocities, collected with varying azimuthal angles, of the crystal platelets at each individual pressure point. This procedure is referred to as individual fit. Individual fits were performed at each pressure point by inverting all the measured acoustic velocities and density data, which were calculated self-consistently from the measured unit-cell volumes. Individual fits converged with small residuals at each pressure point (Figure 3b) thanks to compressional and shear wave velocities being observed for most ranges of rotation angle (χ) and the low correlation between individual elastic stiffness coefficients resulting from the choice of the orientations of the two crystal platelets X1 and X2 used. Uncertainties in the determined c_{ij} values are generally less than 1%, except for c_{12} (< 2%) (Table 2).

Recently, a non-conventional fitting procedure for Brillouin data (referred to as global fit) was proposed by Kurnosov et al. (2017) and described in detail in Buchen (2018). It consists of a global inversion of all sound velocity and density data, instead of independently inverting the data measured at each individual pressure point. This is practically done by fitting all sound velocity and density data with third-order finite strain EoSs describing the evolution with pressure of each c_{ij}, using the formalism of Stixrude and Lithgow-Bertelloni (2005):

$$c_{ijkl} = (1+2f)^{\frac{5}{2}}\left\{c_{ijkl,0} + \left(3K_0c'_{ijkl,0} - 5c_{ijkl,0}\right)f + \left(6K_0c'_{ijkl,0} - 14c_{ijkl,0} - \frac{3}{2}K_0\delta_{kl}^{ij}(3K'_0 - 16)\right)f^2\right\} \quad (4)$$

where c_{ijkl} is the elastic stiffness coefficient in tensorial notation at a given density (i.e., pressure), f is the finite Eulerian strain defined as $\frac{1}{2}\left[\left(\frac{\rho}{\rho_0}\right)^{\frac{2}{3}} - 1\right]$, $c_{ijkl,0}$ is the elastic stiffness coefficient at ambient conditions and $c'_{ijkl,0}$ its pressure derivative, K_0 is the bulk modulus at ambient conditions and K'_0 its pressure derivative, and δ^{ij}_{kl} is equal to −3 for c_{1111}, c_{2222}, and c_{3333} and to −1 for the other six independent components of the elastic tensor. Thus, by refining the ambient-pressure stiffness coefficients ($c_{ij,0}$) and their pressure derivatives ($c'_{ij,0}$), a fit of all measured velocities at all pressure points is obtained. This approach has the advantage that all velocity data from all pressure points are used to constrain the c_{ij}s, minimizing the effect of data scattering on the calculated c_{ij}s and thus reducing their estimated uncertainties (Buchen, 2018). Even though this fitting procedure is particularly suited for very high pressure data, where some of the c_{ij}s are poorly constrained due to the lack of observations (e.g., Criniti et al., 2021), it can be applied to any high-pressure sound velocity dataset and the two procedures should yield consistent results as long as the collected data are of high quality, the high-pressure evolution of all c_{ij} is well described by a third-order finite strain EoS, and no phase transition takes place in the investigated pressure interval. Therefore, we also applied the global fit procedure to our dataset, which yielded very consistent results compared to those obtained by individual fits. The c_{ij}s calculated from two procedures show virtually no discrepancies, with values typically identical within two standard deviations (Table 2, Figure 4).

Because density is measured at each pressure point, it is possible to calculate pressure without relying on a secondary scale (e.g., ruby) using the relative change in volume of the sample, obtained by X-ray diffraction, and the third-order finite strain equations described above. From these, an expression for the isothermal bulk modulus in the Reuss bound (K_{TR}) as a function of volume is obtained and the absolute pressure (P_{abs}) can be calculated by integrating K_{TR}/V over a given volume interval:

$$P_{\text{abs}} = \int_{V_0}^{V} \frac{K_{TR}(V)}{V}\, dV = 3K_{TR0} f (1+2f)^{\frac{5}{2}} \left[1 + \frac{3}{2}(K'_{TR0} - 4) f\right] \quad (5)$$

where K_{TR0} is the bulk modulus at ambient conditions, K'_{TR0} is its pressure derivative, f is the finite Eulerian strain defined as $\frac{1}{2}\left[\left(\frac{V_0}{V}\right)^{\frac{2}{3}} - 1\right]$. The experimentally determined adiabatic bulk modulus K_{SR} (Table 2) was converted into K_{TR} using the relations $K_{SR} = K_{TR}(1 + \alpha\gamma T)$ and $\alpha = \gamma C_V/K_{TR}V$. The thermoelastic parameters used for the conversion are θ_D = 644 K, γ_0 = 1.044 and q = 1.88, corresponding to Fo90 (Angel et al., 2018), and are here assumed to be H_2O-independent. Then, K_{TR0} and K'_{TR0} were calculated by fitting a BM3 EoS to our K_T–V dataset. A comparison between the absolute pressure and the pressures determined from the ruby fluorescence shift is plotted in Supplementary Figure S2, along with the BM3 EoS fits to the K_{SR}–ρ datasets obtained from the global and individual fits, which show excellent agreement.

Figure 4 shows individual c_{ij} as a function of absolute pressure, as well as selected literature data for anhydrous Fo90 olivines for comparison, following the re-analysis of all the published single crystal data proposed by Angel et al. (2018) (Supplementary Table S2). The longitudinal moduli (c_{11}, c_{22} and c_{33}), the off-diagonal moduli (c_{12}, c_{13} and c_{33}) and the shear moduli c_{44} and c_{66} follow a nearly linear increase with pressure, whereas the shear modulus c_{55} exhibits a slightly downward trend towards higher pressures. The longitudinal moduli c_{11}, c_{22}, c_{33} and the shear moduli c_{44}, c_{55}, c_{66} follow similar trends with pressure compared to the anhydrous phase; only c_{66} is slightly offset to lower values in the range of 5 to 10 GPa (Figure 4e). The off-diagonal moduli c_{12}, c_{13}, c_{23} are characterized by very similar values along the whole pressure interval, with the stiffness scheme being $c_{23} > c_{12} > c_{13}$. Due to the small differences in the magnitude of the off-diagonal moduli, their values are frequently the same within uncertainties, especially at high pressure. The off-diagonal moduli c_{12}, c_{13}, c_{23} of the anhydrous phase are scattered but show comparable trends with those of the hydrous phase, especially c_{23}. Even if c_{13} is generally stiffer than c_{12}, in contrast with the hydrous phase, their systematics is more complex, as either they frequently cross over or are the same within uncertainties. Third-order finite strain EoSs (Equation 4) were also used to fit the selected c_{ij} for anhydrous Fo90 olivines (Supplementary Table S2); the determined c_{ij} and c'_{ij} are reported in Table 3. The

longitudinal, shear and off-diagonal moduli of hydrous and anhydrous Fo90 olivines are identical within two standard deviations, and the same holds true for their pressure derivatives, except for c'_{11} of hydrous Fo90 which is slightly larger. The fit curves of the c_{ij}s for hydrous and anhydrous olivine (Supplementary Figure S3) are in good agreement with each other, except for c_{11}, c_{22}, c_{44}, and c_{55} of hydrous Fo90 which become moderately stiffer than their anhydrous corresponding at high pressure; this suggests a relatively small effect of water on the elastic properties of Fo90 olivine.

3.3 Elastic Properties of Hydrous Fo90 *vs* Anhydrous Fo90 Olivine

The adiabatic K_S and G were calculated from the c_{ij} values in the Reuss and Voigt bounds and in the Voigt-Reuss-Hill average at each experimental pressure point and are reported in Table 2. The elastic moduli obtained in this study were then fitted with third-order finite strain EoS to obtain the elastic moduli at ambient conditions (K_{S0} and G_0) and their pressure derivatives (K'_{S0} and G'_0) using the finite strain EoS of Stixrude and Lithgow-Bertelloni (2005):

$$K = (1+2f)^{\frac{5}{2}}\left[K_0 + (3K_0K_0' - 5K_0)f + \frac{27}{2}(K_0K_0' - 4K_0)f^2\right] \quad (6)$$

$$G = (1+2f)^{\frac{5}{2}}\left[G_0 + (3K_0G_0' - 5G_0)f + \left(6K_0G_0' - 24K_0 - 14G_0 + \frac{9}{2}K_0K_0'\right)f^2\right] \quad (7)$$

The EoS parameters for K and G in the Voigt and Reuss bound are reported in Table 4. Both K_S and G show a monotonic increase with pressure (Figure 5a) and are perfectly described by third-order EoS.

To quantify the effect of 0.20 wt.% H_2O on the Fo90 elastic properties, the EoS parameters for hydrous Fo90 olivine determined in this study have to be compared to those of the corresponding anhydrous phase. The elastic behaviour of anhydrous Fo90 olivine has been largely investigated in the past decades and its full elastic tensor has been constrained by a variety of techniques. Angel et al. (2018) presented a re-analysis of all available single crystal data for mantle-composition olivine (Fo90-92) providing best-fit EoS parameters, which were recently used to calculate olivine density profiles over the upper mantle under different thermal regimes (Faccincani et al., 2021). However, a

comparison of the EoS parameters determined in this study with those from Angel et al. (2018) cannot be made for two main reasons: (i) a best fit of the shear modulus data is missing, (ii) the fit includes high-temperature volume data and high-pressure, high-temperature (HP–HT) elasticity data, which are not available for hydrous Fo90 olivine. For this reason, we refitted the high-pressure elasticity data (K_S and G) for anhydrous Fo90 originally used in the fit from Angel et al. (2018) with the same formalism used for hydrous Fo90 olivine (Equations 6 and 7). The data used correspond to Fo90 olivines, and were selected up to ~14 GPa, i.e., the uppermost limit of olivine stability field. In our examination, we also made a re-analysis of the available shear modulus data to provide the best fit for G_0 and G'_0 of anhydrous Fo90 olivine. K_S and G were recalculated from the c_{ij} values reported at high pressure by Abramson et al. (1997) where the data are complete (i.e., four pressure points), the data of Zha et al. (1998) (i.e., four pressure points), the data of Mao et al. (2015) (i.e., seven pressure points) and the data of Zhang and Bass (2016) (i.e., five pressure points) (Figure 5b, Supplementary Table S2). The EoS parameters for K_S and G in the Voigt and Reuss bound are reported in Table 4.

The EoS parameters for hydrous and anhydrous Fo90 olivine at ambient conditions are consistent within errors, especially K and G (Table 4). A comparison of the two obtained sets of EoS parameters indicates that the incorporation of 0.20 wt.% H_2O into the olivine crystal structure causes only a minor reduction in K_{S0} and G_0 of ~0.2% and ~0.7%, respectively, and an increase in K'_{S0} and G'_0 of ~2.5% and ~5%, respectively. This suggests a negligible effect of water incorporation on K and G of Fo90 olivine and a moderate, positive effect on K' and G'. For this reason, the elastic behaviour of hydrous and anhydrous Fo90 olivine is indistinguishable within uncertainties up to ~14 GPa. This is consistent with a recent high-pressure single-crystal X-ray diffraction study conducted on a sample of Fo95 olivine with a low water content (~0.15 wt.% H_2O) (Xu et al., 2020), where hydrogen substitution is predominantly associated with the T site. As the effect of water on the elastic moduli and their derivatives in our Fo90 and Fo100 (Mao et al., 2010) may also depend on different H substitution mechanisms in olivine, besides distinct water contents, comparisons among different data should be made carefully. The Fo100 single crystals studied by Mao et al. (2010) were synthesized by Smyth

et al. (2006), run SZ0408A, to which the reader is referred for synthesis conditions and FTIR spectrum. For this sample, it was suggested that hydration predominantly occurred through the octahedral substitution $Mg^{2+} \leftrightarrow 2H^{+}$. On the other hand, a tetrahedral substitution $Si^{4+} \leftrightarrow 4H^{+}$ has been suggested for our sample (Withers et al., 2011). Note, however, that the FTIR spectra of hydrous Fo100 (Smyth et al., 2006, Figure 2) and hydrous Fo90 (Withers et al., 2011, Figure 2) both show strong absorbance features in the identical high wavenumber region, hinting that the two samples should present the same substitution mechanism. Various pieces of evidence suggest that absorption features in the high wavenumber region (~3.450-3.600 cm^{-1}) are related to OH bonding to T sites (Fei and Katsura, 2020; Umemoto et al., 2011; Xue et al., 2017), therefore we may expect that both the Fo100 and Fo90 sample contain predominantly Si vacancies. The important observation, however, for the aim of this study is that both samples present the same type of defects and therefore we can compare the effect of hydration on their elastic properties directly, upon normalization with respect to H_2O concentration. The effect of water on the elastic parameters can be then expressed as:

$$\Delta_{H_2O}M\left(\frac{[M]}{wt.\%\ H_2O}\right) = \frac{M_{hydrous} - M_{dry}}{X_{H_2O}(wt.\%)} \quad (8)$$

where M can be K_{S0}, G_0 (in GPa), K'_{S0} or G'_0 (non-dimensional) and X_{H2O} is the water content of the hydrous sample in wt.%. Δ_{H2O}M values defined in this fashion yield the change in elastic properties for a reference water content of 1 wt.%; the obtained results for both Fo90 and Fo100 are reported in Table 4. Δ_{H2O}M values are affected by large uncertainties, especially in the case of Fo90. This mostly arises from the fitting parameters of anhydrous Fo90, which are less well-constrained because four different datasets were combined in the EoS fit of the elastic moduli (Table 4). $\Delta_{H2O}K_{S0}$ and $\Delta_{H2O}G_{S0}$ for Fo90 and Fo100 are on the margins of being mutually consistent. Contrary to the prediction by Jacobsen et al. (2008, 2009), K_{S0} of Fo100 is slightly more reduced by H_2O compared to Fo90 and the two G_0's show similar reductions. However, $\Delta_{H2O}K'_{S0}$ and $\Delta_{H2O}G'_{S0}$ values are in excellent agreement within mutual uncertainties (Table 4). Therefore, the more pronounced effect observed by Mao et al. (2010) on hydrous Fo100 elastic properties arises by virtue of the higher water content,

and not from a different effect of water in Fe-free and Fe-bearing samples as shown in Table 4. This also suggests that hydration is most likely to have a linear effect on the pressure derivatives of olivines.

3.4 Effect of Hydration on Sound Wave Velocities of Fo90 Olivine and its Geophysical Implications

Using the new experimental data obtained in this study, we calculated the aggregate sound wave velocities of hydrous Fo90 olivine with 0.20 wt.% H_2O as a function of pressure. Aggregate sound wave velocities of anhydrous Fo90 olivine are compared with those for hydrous olivine (Figure 6). As the effect of temperature on the elasticity of hydrous olivine is currently unknown, all the calculations were performed at 300 K. In this context, Ye et al. (2009) showed that the thermal expansion coefficient of hydrous (0.89 wt.% H_2O) end-member forsterite (Fo100) is marginally larger, ~4.5(2.6) %, than that of Fo100. If this applies also for Fo90, the lower water content of our hydrous olivine (0.20 wt.% H_2O) would have a negligible effect on its thermal expansion. Moreover, the effect of water on the thermal expansion of hydrous (~2.5 wt.% H_2O) wadsleyite and ringwoodite, i.e., the high-pressure polymorphs of olivine, seems to be negligible (Inoue et al., 2004). Therefore, we propose that H_2O is unlikely to have a significant effect on the thermal expansion of olivine.

The v_P and v_S of hydrous Fo90 follow similar trends to those of the elastic moduli (Figure 6), with velocities being consistent with those of anhydrous Fo90up to ~14 GPa. Mao et al. (2010) showed that v_P and v_S of the hydrous Fo100 cross and exceed those of the corresponding anhydrous phase at about 4 and 3 GPa, respectively, and rapidly diverge at higher pressure. The prominent rise of v_P and v_S with increasing pressure is due to the higher water content of the hydrous Fo100 sample employed by Mao et al. (2010) and not to a different effect of water in Fe-free and Fe-bearing samples, as shown in Table 4.

The 410-km global seismic discontinuity is widely accepted to be caused by the phase transition of olivine to its high pressure polymorph wadsleyite (Frost, 2008). Several works attempted to

406 constrain the bulk olivine content in the upper mantle by comparing sound wave velocities of olivine
407 and wadsleyite, calculated from either experimental or computational mineral physics data, with the
408 observed seismic velocity contrasts across the discontinuity (e.g., Bass and Anderson, 1984;
409 Dziewonski and Anderson, 1981; Núñez-Valdez et al., 2013; Wang et al., 2014, 2019). However, the
410 calculated velocity contrasts across the discontinuity for a pyrolite composition (~60 vol.% olivine)
411 are not consistent with global 1-D seismic models (e.g., Preliminary Earth Reference Model, PREM,
412 or AK135; Dziewonski and Anderson, 1981; Kennett et al., 1995), pointing towards a bottom upper
413 mantle that is less olivine-rich than pyrolite. Considering the reduction of the sound wave velocities
414 of wadsleyite due to the incorporation of water (Mao et al., 2008a, 2008b), it was proposed that water
415 dissolved in olivine and wadsleyite may reconcile the pyrolite model with seismological observations.
416 Water is preferentially partitioned in wadsleyite ($D_{wad/ol}$ = 6; Thio et al., 2016) and whether the
417 presence of water can resolve seismological observations with pyrolitic mantle olivine contents will
418 depend on both the expected amount of water in olivine and to what extents it affects v_P and v_S of
419 olivine. Available experimental data for hydrous olivine indicate storage capacities up to 0.9 wt.%
420 (Smyth et al., 2006), but the water content of olivine under relevant deep upper mantle conditions
421 will be much lower, around 0.2 – 0.5 wt.% H_2O (e.g., Férot and Bolfan-Casanova, 2012; Hirschmann
422 et al., 2005; Mosenfelder, 2006). In this regard, our data are particularly significant and indicate that
423 the incorporation of ~0.20 wt.% H_2O into Fo90 olivine crystal structure does not significantly affect
424 its v_P and v_S at high pressure. To explore whether the presence of higher water contents in olivine
425 would cause greater effects on its v_P and v_S, $\Delta_{H2O}M$ values obtained for Fo90 were scaled to 0.5 wt.%
426 H_2O to determine the variations in *K*, *K'*, *G* and *G'* associated with the incorporation of such amount
427 of water and calculate the sound velocities of Fo90 hosting 0.5 wt.% H_2O (Table 4, Figures 5c-6c).
428 Because hydration causes an increase in the unit-cell volume, the room pressure volume of Fo90 with
429 0.5 wt.% H_2O was estimated using the expression $V_{0\ hydrous}$ [Å^3] = $V_{0\ anhydrous}$ [Å^3] + 5.5 x 10^{-5} [Å^3] x
430 H_2O [ppm] from Smyth et al. (2006); $V_{0\ anhydrous}$ was calculated using the same expression solved with
431 the data of the hydrous olivine from this study (i.e., V_0 = 291.65(2) Å^3 and ~2000 ppm). Then, the

resulting volume of Fo90 with 0.5 wt.% H_2O was converted into density. The calculated sound wave velocities for Fo90 with 0.5 wt.% H_2O are reported in Figure 6c and compared to those of hydrous Fo90 with 0.20 wt.% H_2O and anhydrous Fo90. The incorporation of 0.5 wt.% H_2O into Fo90 olivine slightly reduces its elastic moduli (mostly G) and sound wave velocities at ambient pressure (Table 4, Figures 5c-6c). Nonetheless, v_P and v_S of the hydrous phase become indistinguishable within uncertainties with those of the anhydrous phase at pressures exceeding ~2 and ~5 GPa, owing to the larger K'_{S0} and G'_0. This advises caution when speculating on the water content in the deep upper mantle based on its effect on olivine elastic properties and seismic wave velocities. Furthermore, our data also suggest that H_2O incorporation in olivine may not reconcile seismological observations at the 410-km discontinuity with a pyrolitic mantle, although we are aware that direct determinations of sound wave velocities of hydrous olivine and hydrous wadsleyite at combined HP–HT (e.g., Buchen et al., 2018) are needed to refine these findings.

The discrepancy between the observed and calculated wave velocities for a pyrolite composition may also arise from strong variations of olivine content and upper mantle lithologies near the 410-km seismic discontinuity, for which corroborating evidence has been found by Zhang and Bass (2016). Indeed, olivine contents inferred from regional seismic models of the Pacific region are extremely variable and increase from approximately 20 – 40 % in the central Pacific to 60 – 90 % in the western U.S. and eastern Pacific regions. Given the indistinguishable seismic behaviour of hydrous and anhydrous Fo90 olivine at high pressure, we argue that this high degree of heterogeneity does not stem from the potentially different responses of dry and wet regions of the deep upper mantle, but rather may arise from variations in olivine content.

4. Concluding remarks

The sound velocities and single-crystal elastic coefficients of Fo90 olivine with 0.20 wt.% H_2O were measured up to ~12 GPa at room temperature by simultaneous single-crystal X-ray diffraction and Brillouin scattering experiments. Compared to the anhydrous phase, K and G of hydrous Fo90 at ambient conditions are virtually identical, while their pressure derivatives are slightly larger, although

458 consistent within mutual uncertainties. For this reason, the elastic behaviour of hydrous and
459 anhydrous Fo90 olivine is indistinguishable within uncertainties up to pressures corresponding to the
460 base of the upper mantle. Using our new accurate data, we investigated the effect of hydration on
461 aggregate sound velocities of Fo90. At ambient pressure, the compressional and shear wave velocities
462 of hydrous Fo90 with 0.2 and 0.5 wt.% H_2O are identical to, or slightly slower than, those of the
463 anhydrous phase. In both cases however, v_P and v_S of the hydrous and anhydrous phases are
464 indistinguishable within uncertainties at deep upper mantle conditions. Therefore, if amounts of water
465 were to be incorporated into Fo90 olivine crystal structure, its elastic and seismic behaviour at high
466 pressure may remain unchanged. Based on our findings, we suggest that water in olivine is not
467 seismically detectable, at least for contents up to 0.2 – 0.5 wt.%, i.e., the amount of water expected
468 in olivine at deep upper mantle conditions. We therefore advise caution about speculations of the
469 water content in the deep upper mantle based on its effect on olivine elastic properties and sound
470 wave velocities. In addition, our data also suggest that the hydration of olivine is unlikely to be a key
471 factor in reconciling seismic velocity and density contrasts across the 410-km discontinuity with a
472 pyrolitic mantle.

473 ## Author contribution statement

474 [L.F.] Conceptualization, Methodology, Formal analysis, Investigation, Data Curation, Writing–
475 Original Draft, Writing–Review & Editing; [G.C.]: Methodology, Formal analysis, Investigation,
476 Data Curation, Writing–Review & Editing; [A.K.]: Methodology, Investigation, Writing–Review &
477 Editing; [T.B.B.]: Methodology, Investigation, Writing–Review & Editing, Supervision; [A.W.]:
478 Investigation, Writing–Review & Editing; [M.M.]: Writing–Review & Editing, Supervision; [F.N.]:
479 Writing–Review & Editing, Supervision; [M.C.]: Conceptualization, Writing–Review & Editing,
480 Supervision.

Declaration of Competing Interest

The authors declare that they have no known competing financial interests or personal relationships that could have appeared to influence the work reported in this paper.

Acknowledgements

The authors would like to thank R. Njul for his help in double–side polishing the two single crystals to platelets and D. Wiesner for her help in the operation of the FIB device. L.F. acknowledges Istituto Nazionale di Geofisica e Vulcanologia (INGV) for funding his Ph.D. project (XXXV cycle) with thematic ‘Links between rheology, mineralogy and composition of the Earth's mantle’ and the University of Ferrara for the 2021 IUSS international mobility program. This research was also supported by the Italian National Research Program (PRIN Grant 20178LPCPW ’Micro to Macro – How to unravel the nature of the Large Magmatic Events' to M.C.)

Data Availability

All data derived from this research are presented in the enclosed tables, figures, and supplementary material.

References

Abramson, E.H., Brown, J.M., Slutsky, L.J., Zaug, J., 1997. The elastic constants of San Carlos olivine to 17 GPa. J. Geophys. Res. Solid Earth 102, 12253–12263. https://doi.org/10.1029/97JB00682

Angel, R.J., 2000. Equations of State. Rev. Mineral. Geochemistry 41, 35–59. https://doi.org/10.2138/rmg.2000.41.2

Angel, R.J., Alvaro, M., Gonzalez-Platas, J., 2014. EosFit7c and a Fortran module (library) for equation of state calculations. Zeitschrift für Krist. - Cryst. Mater. 229, 405–419. https://doi.org/10.1515/zkri-2013-1711

504 Angel, R.J., Alvaro, M., Nestola, F., 2018. 40 years of mineral elasticity: a critical review and a new
505 parameterisation of equations of state for mantle olivines and diamond inclusions. Phys. Chem.
506 Miner. 45, 95–113. https://doi.org/10.1007/s00269-017-0900-7

507 Angel, R.J., Finger, L.W., 2011. SINGLE : a program to control single-crystal diffractometers. J.
508 Appl. Crystallogr. 44, 247–251. https://doi.org/10.1107/S0021889810042305

509 Bali, E., Bolfan-Casanova, N., Koga, K.T., 2008. Pressure and temperature dependence of H
510 solubility in forsterite: An implication to water activity in the Earth interior. Earth Planet. Sci.
511 Lett. 268, 354–363. https://doi.org/10.1016/j.epsl.2008.01.035

512 Bass, J.D., Anderson, D.L., 1984. Composition of the upper mantle: Geophysical tests of two
513 petrological models. Geophys. Res. Lett. 11, 229–232.
514 https://doi.org/10.1029/GL011i003p00229

515 Bell, D.R., Rossman, G.R., 1992. Water in Earth's Mantle: The Role of Nominally Anhydrous
516 Minerals. Science (80-.). 255, 1391–1397. https://doi.org/10.1126/science.255.5050.1391

517 Beran, A., Libowitzky, E., 2006. Water in natural mantle minerals II: Olivine, garnet and accessory
518 minerals, in: Reviews in Mineralogy and Geochemistry 62: Water in Nominally Anhydrous
519 Minerals. pp. 169–192. https://doi.org/10.2138/rmg.2006.62.8

520 Boehler, R., De Hantsetters, K., 2004. New anvil designs in diamond-cells. High Press. Res. 24, 391–
521 396. https://doi.org/10.1080/08957950412331323924

522 Bonadiman, C., Hao, Y., Coltorti, M., Dallai, L., Faccini, B., Huang, Y.X., 2009. Water contents of
523 pyroxenes in intraplate lithospheric mantle. Eur. J. Mineral. 21, 637–647.
524 https://doi.org/10.1127/0935-1221/2009/0021-1935

525 Brodholt, J.P., Refson, K., 2000. An ab initio study of hydrogen in forsterite and a possible
526 mechanism for hydrolytic weakening. J. Geophys. Res. Solid Earth 105, 18977–18982.
527 https://doi.org/10.1029/2000JB900057

Buchen, J., 2018. The Elastic Properties of Wadsleyite and Stishovite at High Pressures: Tracing Deep Earth Material Cycles. University of Bayreuth. https://doi.org/10.15495/EPub_UBT_00004410

Buchen, J., Marquardt, H., Speziale, S., Kawazoe, T., Boffa Ballaran, T., Kurnosov, A., 2018. High-pressure single-crystal elasticity of wadsleyite and the seismic signature of water in the shallow transition zone. Earth Planet. Sci. Lett. 498, 77–87. https://doi.org/10.1016/j.epsl.2018.06.027

Chang, Y.-Y., Hsieh, W.-P., Tan, E., Chen, J., 2017. Hydration-reduced lattice thermal conductivity of olivine in Earth's upper mantle. Proc. Natl. Acad. Sci. 114, 4078–4081. https://doi.org/10.1073/pnas.1616216114

Costa, F., Chakraborty, S., 2008. The effect of water on Si and O diffusion rates in olivine and implications for transport properties and processes in the upper mantle. Phys. Earth Planet. Inter. 166, 11–29. https://doi.org/10.1016/j.pepi.2007.10.006

Criniti, G., Kurnosov, A., Boffa Ballaran, T., Frost, D.J., 2021. Single-Crystal Elasticity of MgSiO 3 Bridgmanite to Mid-Lower Mantle Pressure. J. Geophys. Res. Solid Earth 126. https://doi.org/10.1029/2020JB020967

Demouchy, S., Jacobsen, S.D., Gaillard, F., Stern, C.R., 2006. Rapid magma ascent recorded by water diffusion profiles in mantle olivine. Geology 34, 429. https://doi.org/10.1130/G22386.1

Demouchy, S., Mackwell, S., 2006. Mechanisms of hydrogen incorporation and diffusion in iron-bearing olivine. Phys. Chem. Miner. 33, 347–355. https://doi.org/10.1007/s00269-006-0081-2

Downs, R.T., Zha, C.-S., Duffy, T.S., Finger, L.W., 1996. The equation of state of forsterite to 17.2 GPa and effects of pressure media. Am. Mineral. 81, 51–55. https://doi.org/10.2138/am-1996-1-207

Dziewonski, A.M., Anderson, D.L., 1981. Preliminary reference Earth model. Phys. Earth Planet. Inter. 25, 297–356. https://doi.org/10.1016/0031-9201(81)90046-7

552 Faccincani, L., Faccini, B., Casetta, F., Mazzucchelli, M., Nestola, F., Coltorti, M., 2021. EoS of
553 mantle minerals coupled with composition and thermal state of the lithosphere: Inferring the
554 density structure of peridotitic systems. Lithos 404–405, 106483.
555 https://doi.org/10.1016/j.lithos.2021.106483

556 Fei, H., Katsura, T., 2020. Pressure Dependence of Proton Incorporation and Water Solubility in
557 Olivine. J. Geophys. Res. Solid Earth 125, 1–13. https://doi.org/10.1029/2019JB018813

558 Férot, A., Bolfan-Casanova, N., 2012. Water storage capacity in olivine and pyroxene to 14GPa:
559 Implications for the water content of the Earth's upper mantle and nature of seismic
560 discontinuities. Earth Planet. Sci. Lett. 349–350, 218–230.
561 https://doi.org/10.1016/j.epsl.2012.06.022

562 Frost, D.J., 2008. The Upper Mantle and Transition Zone. Elements 4, 171–176.
563 https://doi.org/10.2113/GSELEMENTS.4.3.171

564 Hirschmann, M.M., Aubaud, C., Withers, A.C., 2005. Storage capacity of H2O in nominally
565 anhydrous minerals in the upper mantle. Earth Planet. Sci. Lett. 236, 167–181.
566 https://doi.org/10.1016/j.epsl.2005.04.022

567 Hushur, A., Manghnani, M.H., Smyth, J.R., Nestola, F., Frost, D.J., 2009. Crystal chemistry of
568 hydrous forsterite and its vibrational properties up to 41 GPa. Am. Mineral. 94, 751–760.
569 https://doi.org/10.2138/am.2009.2990

570 Inoue, T., 1994. Effect of water on melting phase relations and melt composition in the system
571 Mg2SiO4-MgSiO3-H2O up to 15 GPa. Phys. Earth Planet. Inter. 85, 237–263.
572 https://doi.org/10.1016/0031-9201(94)90116-3

573 Inoue, T., Tanimoto, Y., Irifune, T., Suzuki, T., Fukui, H., Ohtaka, O., 2004. Thermal expansion of
574 wadsleyite, ringwoodite, hydrous wadsleyite and hydrous ringwoodite. Phys. Earth Planet. Inter.
575 143–144, 279–290. https://doi.org/10.1016/j.pepi.2003.07.021

576 Jacobsen, S.D., Jiang, F., Mao, Z., Duffy, T.S., Smyth, J.R., Holl, C.M., Frost, D.J., 2009. Correction
577 to “Effects of hydration on the elastic properties of olivine.” Geophys. Res. Lett. 36, L12302.
578 https://doi.org/10.1029/2009GL038660

579 Jacobsen, S.D., Jiang, F., Mao, Z., Duffy, T.S., Smyth, J.R., Holl, C.M., Frost, D.J., 2008. Effects of
580 hydration on the elastic properties of olivine. Geophys. Res. Lett. 35, L14303.
581 https://doi.org/10.1029/2008GL034398

582 Jung, H., Karato, S.-I., 2001. Effects of water on dynamically recrystallized grain-size of olivine. J.
583 Struct. Geol. 23, 1337–1344. https://doi.org/10.1016/S0191-8141(01)00005-0

584 Kantor, I., Prakapenka, V., Kantor, A., Dera, P., Kurnosov, A., Sinogeikin, S., Dubrovinskaia, N.,
585 Dubrovinsky, L., 2012. BX90: A new diamond anvil cell design for X-ray diffraction and optical
586 measurements. Rev. Sci. Instrum. 83, 125102. https://doi.org/10.1063/1.4768541

587 Kennett, B.L.N., Engdahl, E.R., Buland, R., 1995. Constraints on seismic velocities in the Earth from
588 traveltimes. Geophys. J. Int. 122, 108–124. https://doi.org/10.1111/j.1365-
589 246X.1995.tb03540.x

590 King, H.E., Finger, L.W., 1979. Diffracted beam crystal centering and its application to high-pressure
591 crystallography. J. Appl. Crystallogr. 12, 374–378.
592 https://doi.org/10.1107/S0021889879012723

593 Kurnosov, A., Kantor, I., Boffa-Ballaran, T., Lindhardt, S., Dubrovinsky, L., Kuznetsov, A., Zehnder,
594 B.H., 2008. A novel gas-loading system for mechanically closing of various types of diamond
595 anvil cells. Rev. Sci. Instrum. 79, 045110. https://doi.org/10.1063/1.2902506

596 Kurnosov, A., Marquardt, H., Frost, D.J., Ballaran, T.B., Ziberna, L., 2017. Evidence for a Fe3+-rich
597 pyrolitic lower mantle from (Al,Fe)-bearing bridgmanite elasticity data. Nature 543, 543–546.
598 https://doi.org/10.1038/nature21390

599 Mao, Z., Fan, D., Lin, J.-F., Yang, J., Tkachev, S.N., Zhuravlev, K., Prakapenka, V.B., 2015.

Elasticity of single-crystal olivine at high pressures and temperatures. Earth Planet. Sci. Lett. 426, 204–215. https://doi.org/10.1016/j.epsl.2015.06.045

Mao, Z., Jacobsen, S.D., Jiang, F., Smyth, J.R., Holl, C.M., Duffy, T.S., 2008a. Elasticity of hydrous wadsleyite to 12 GPa: Implications for Earth's transition zone. Geophys. Res. Lett. 35, L21305. https://doi.org/10.1029/2008GL035618

Mao, Z., Jacobsen, S.D., Jiang, F., Smyth, J.R., Holl, C.M., Frost, D.J., Duffy, T.S., 2010. Velocity crossover between hydrous and anhydrous forsterite at high pressures. Earth Planet. Sci. Lett. 293, 250–258. https://doi.org/10.1016/j.epsl.2010.02.025

Mao, Z., Jacobsen, S.D., Jiang, F.M., Smyth, J.R., Holl, C.M., Frost, D.J., Duffy, T.S., 2008b. Single-crystal elasticity of wadsleyites, β-Mg2SiO4, containing 0.37–1.66 wt.% H2O. Earth Planet. Sci. Lett. 268, 540–549. https://doi.org/10.1016/j.epsl.2008.01.023

Matveev, S., O'neill, H.S.C., Ballhaus, C., Taylor, W.R., Green, D.H., 2001. Effect of Silica Activity on OH- IR Spectra of Olivine: Implications for Low-aSiO2 Mantle Metasomatism. J. Petrol. 42, 721–729. https://doi.org/10.1093/petrology/42.4.721

Mosenfelder, J.L., 2006. Hydrogen incorporation in olivine from 2-12 GPa. Am. Mineral. 91, 285–294. https://doi.org/10.2138/am.2006.1943

Nestola, F., Nimis, P., Ziberna, L., Longo, M., Marzoli, A., Harris, J.W., Manghnani, M.H., Fedortchouk, Y., 2011. First crystal-structure determination of olivine in diamond: Composition and implications for provenance in the Earth's mantle. Earth Planet. Sci. Lett. 305, 249–255. https://doi.org/10.1016/j.epsl.2011.03.007

Novella, D., Bolfan-Casanova, N., Nestola, F., Harris, J.W., 2015. H2O in olivine and garnet inclusions still trapped in diamonds from the Siberian craton: Implications for the water content of cratonic lithosphere peridotites. Lithos 230, 180–183. https://doi.org/10.1016/j.lithos.2015.05.013

624 Núñez-Valdez, M., Wu, Z., Yu, Y.G., Wentzcovitch, R.M., 2013. Thermal elasticity of (Fe x ,Mg 1−
625 x) 2 SiO 4 olivine and wadsleyite. Geophys. Res. Lett. 40, 290–294.
626 https://doi.org/10.1002/grl.50131

627 Nye, J.F., 1985. Physical properties of crystals: their representation by tensors and matrices. Oxford
628 university press.

629 Pamato, M.G., Nestola, F., Novella, D., Smyth, J.R., Pasqual, D., Gatta, G.D., Alvaro, M., Secco, L.,
630 2019. The High-Pressure Structural Evolution of Olivine along the Forsterite–Fayalite Join.
631 Minerals 9, 790. https://doi.org/10.3390/min9120790

632 Peslier, A.H., 2010. A review of water contents of nominally anhydrous natural minerals in the
633 mantles of Earth, Mars and the Moon. J. Volcanol. Geotherm. Res. 197, 239–258.
634 https://doi.org/10.1016/j.jvolgeores.2009.10.006

635 Peslier, A.H., Woodland, A.B., Bell, D.R., Lazarov, M., 2010. Olivine water contents in the
636 continental lithosphere and the longevity of cratons. Nature 467, 78–81.
637 https://doi.org/10.1038/nature09317

638 Peslier, A.H., Woodland, A.B., Wolff, J.A., 2008. Fast kimberlite ascent rates estimated from
639 hydrogen diffusion profiles in xenolithic mantle olivines from southern Africa. Geochim.
640 Cosmochim. Acta 72, 2711–2722. https://doi.org/10.1016/j.gca.2008.03.019

641 Ralph, R.L., Finger, L.W., 1982. A computer program for refinement of crystal orientation matrix
642 and lattice constants from diffractometer data with lattice symmetry constraints. J. Appl.
643 Crystallogr. 15, 537–539. https://doi.org/10.1107/S0021889882012539

644 Regenauer-Lieb, K., 2006. Water and Geodynamics. Rev. Mineral. Geochemistry 62, 451–473.
645 https://doi.org/10.2138/rmg.2006.62.19

646 Ringwood, A.E., 1975. Composition and Petrology of the Earth's Mantle, Mac Graw-Hill Book
647 Company.

Sandercock, J.R., 1982. Trends in brillouin scattering: Studies of opaque materials, supported films, and central modes, in: Cardona, M., Güntherodt, G. (Eds.), Light Scattering in Solids III: Recent Results. Springer Berlin Heidelberg, Berlin, Heidelberg, pp. 173–206. https://doi.org/10.1007/3540115137_6

Schulze, K., Buchen, J., Marquardt, K., Marquardt, H., 2017. Multi-sample loading technique for comparative physical property measurements in the diamond-anvil cell. High Press. Res. 37, 159–169. https://doi.org/10.1080/08957959.2017.1299719

Shen, G., Wang, Y., Dewaele, A., Wu, C., Fratanduono, D.E., Eggert, J., Klotz, S., Dziubek, K.F., Loubeyre, P., Fat'yanov, O. V., Asimow, P.D., Mashimo, T., Wentzcovitch, R.M.M., 2020. Toward an international practical pressure scale: A proposal for an IPPS ruby gauge (IPPS-Ruby2020). High Press. Res. 40, 299–314. https://doi.org/10.1080/08957959.2020.1791107

Smyth, J.R., Frost, D.J., Nestola, F., Holl, C.M., Bromiley, G., 2006. Olivine hydration in the deep upper mantle: Effects of temperature and silica activity. Geophys. Res. Lett. 33, L15301. https://doi.org/10.1029/2006GL026194

Speziale, S., Marquardt, H., Duffy, T.S., 2014. Brillouin Scattering and its Application in Geosciences, in: Reviews in Mineralogy and Geochemistry. pp. 543–603. https://doi.org/10.2138/rmg.2014.78.14

Stixrude, L., Lithgow-Bertelloni, C., 2005. Thermodynamics of mantle minerals - I. Physical properties. Geophys. J. Int. 162, 610–632. https://doi.org/10.1111/j.1365-246X.2005.02642.x

Thio, V., Cobden, L., Trampert, J., 2016. Seismic signature of a hydrous mantle transition zone. Phys. Earth Planet. Inter. 250, 46–63. https://doi.org/10.1016/j.pepi.2015.11.005

Trots, D.M., Kurnosov, A., Ballaran, T.B., Tkachev, S., Zhuravlev, K., Prakapenka, V., Berkowski, M., Frost, D.J., 2013. The Sm:YAG primary fluorescence pressure scale. J. Geophys. Res. Solid Earth 118, 5805–5813. https://doi.org/10.1002/2013JB010519

672 Trots, D.M., Kurnosov, A., Vasylechko, L., Berkowski, M., Boffa Ballaran, T., Frost, D.J., 2011.
673 Elasticity and equation of state of Li2B4O7. Phys. Chem. Miner. 38, 561–567.
674 https://doi.org/10.1007/s00269-011-0428-1

675 Umemoto, K., Wentzcovitch, R.M., Hirschmann, M.M., Kohlstedt, D.L., Withers, A.C., 2011. A
676 first-principles investigation of hydrous defects and IR frequencies in forsterite: The case for Si
677 vacancies. Am. Mineral. 96, 1475–1479. https://doi.org/10.2138/am.2011.3720

678 Wang, J., Bass, J.D., Kastura, T., 2014. Elastic properties of iron-bearing wadsleyite to 17.7GPa:
679 Implications for mantle mineral models. Phys. Earth Planet. Inter. 228, 92–96.
680 https://doi.org/10.1016/j.pepi.2014.01.015

681 Wang, W., Walter, M.J., Peng, Y., Redfern, S., Wu, Z., 2019. Constraining olivine abundance and
682 water content of the mantle at the 410-km discontinuity from the elasticity of olivine and
683 wadsleyite. Earth Planet. Sci. Lett. 519, 1–11. https://doi.org/10.1016/j.epsl.2019.04.018

684 Whitfield, C.H., Brody, E.M., Bassett, W.A., 1976. Elastic moduli of NaCl by Brillouin scattering at
685 high pressure in a diamond anvil cell. Rev. Sci. Instrum. 47, 942–947.
686 https://doi.org/10.1063/1.1134778

687 Withers, A.C., Bureau, H., Raepsaet, C., Hirschmann, M.M., 2012. Calibration of infrared
688 spectroscopy by elastic recoil detection analysis of H in synthetic olivine. Chem. Geol. 334, 92–
689 98. https://doi.org/10.1016/j.chemgeo.2012.10.002

690 Withers, A.C., Hirschmann, M.M., 2008. Influence of temperature, composition, silica activity and
691 oxygen fugacity on the H2O storage capacity of olivine at 8 GPa. Contrib. to Mineral. Petrol.
692 156, 595–605. https://doi.org/10.1007/s00410-008-0303-3

693 Withers, A.C., Hirschmann, M.M., Tenner, T.J., 2011. The effect of Fe on olivine H2O storage
694 capacity: Consequences for H2O in the martian mantle. Am. Mineral. 96, 1039–1053.
695 https://doi.org/10.2138/am.2011.3669

696 Xia, Q.-K., Hao, Y., Li, P., Deloule, E., Coltorti, M., Dallai, L., Yang, X., Feng, M., 2010. Low water
697 content of the Cenozoic lithospheric mantle beneath the eastern part of the North China Craton.
698 J. Geophys. Res. 115, B07207. https://doi.org/10.1029/2009JB006694

699 Xu, J., Fan, D., Zhang, D., Li, B., Zhou, W., Dera, P.K., 2020. Investigation of the crystal structure
700 of a low water content hydrous olivine to 29.9 GPa: A high-pressure single-crystal X-ray
701 diffraction study. Am. Mineral. 105, 1857–1865. https://doi.org/10.2138/am-2020-7444

702 Xue, X., Kanzaki, M., Turner, D., Loroch, D., 2017. Hydrogen incorporation mechanisms in
703 forsterite: New insights from 1 H and 29 Si NMR spectroscopy and first-principles calculation.
704 Am. Mineral. 102, 519–536. https://doi.org/10.2138/am-2017-5878

705 Ye, Y., Schwering, R.A., Smyth, J.R., 2009. Effects of hydration on thermal expansion of forsterite,
706 wadsleyite, and ringwoodite at ambient pressure. Am. Mineral. 94, 899–904.
707 https://doi.org/10.2138/am.2009.3122

708 Zha, C., Duffy, T.S., Downs, R.T., Mao, H., Hemley, R.J., 1998. Brillouin scattering and X-ray
709 diffraction of San Carlos olivine: direct pressure determination to 32 GPa. Earth Planet. Sci.
710 Lett. 159, 25–33. https://doi.org/10.1016/S0012-821X(98)00063-6

711 Zhang, J.S., Bass, J.D., 2016. Sound velocities of olivine at high pressures and temperatures and the
712 composition of Earth's upper mantle. Geophys. Res. Lett. 43, 9611–9618.
713 https://doi.org/10.1002/2016GL069949

714

Figures

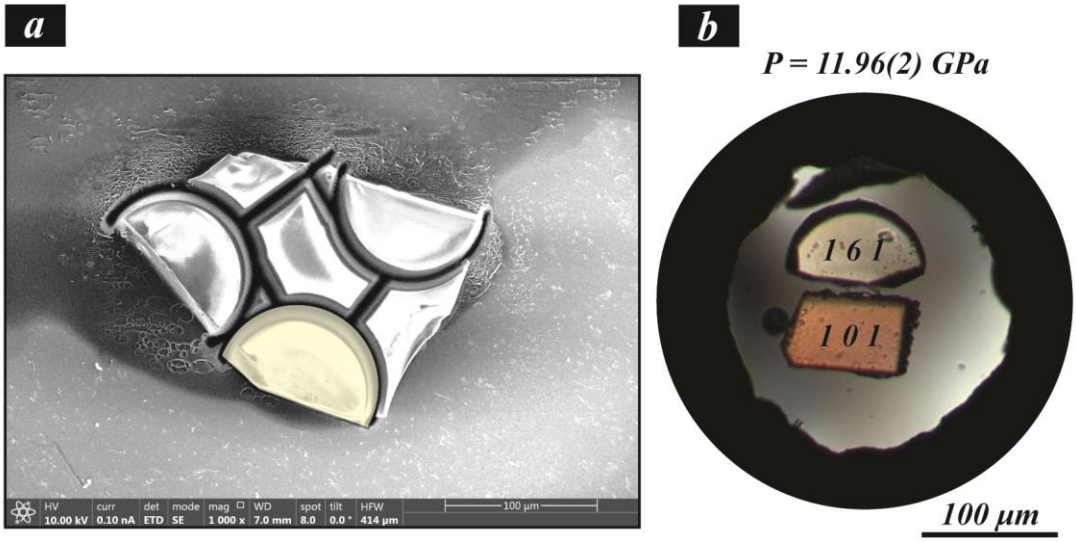
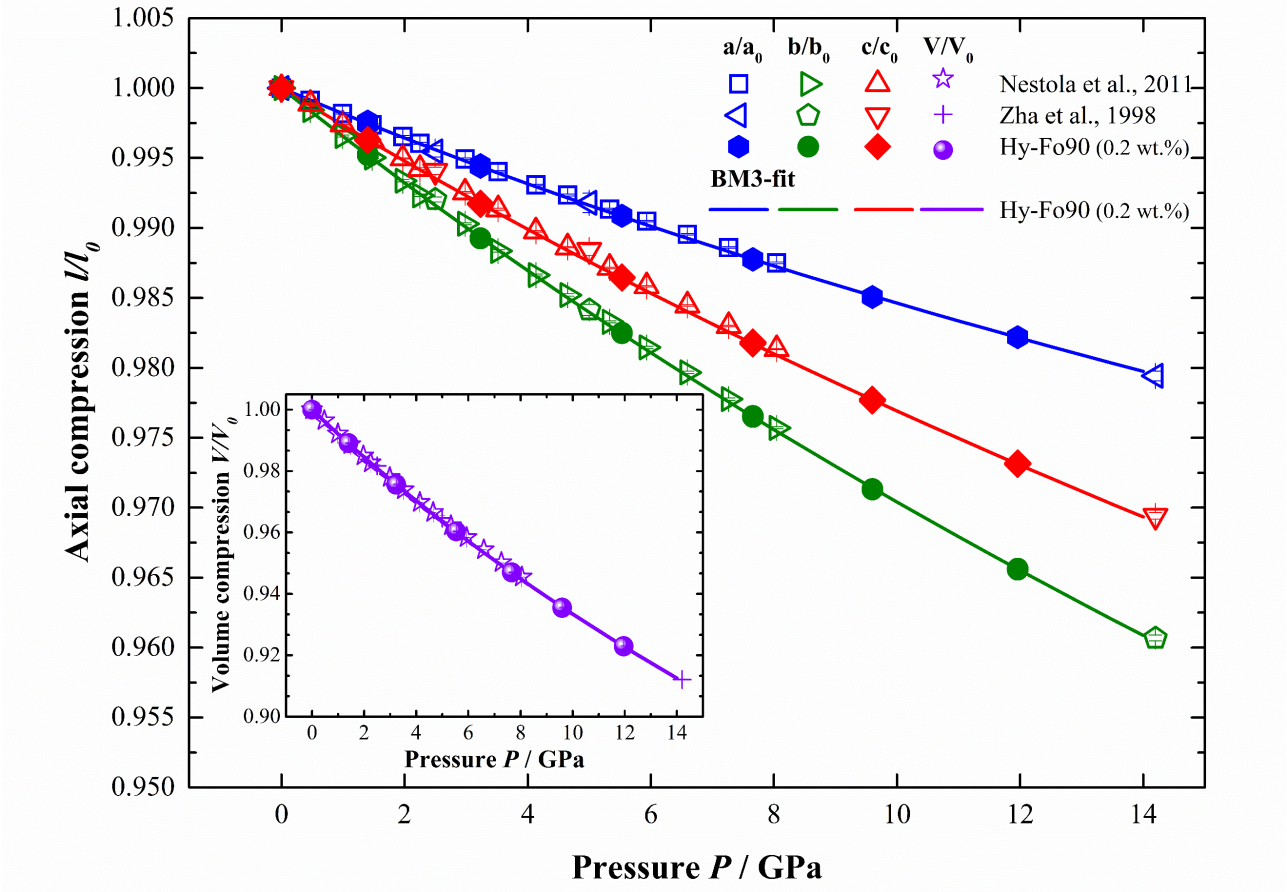
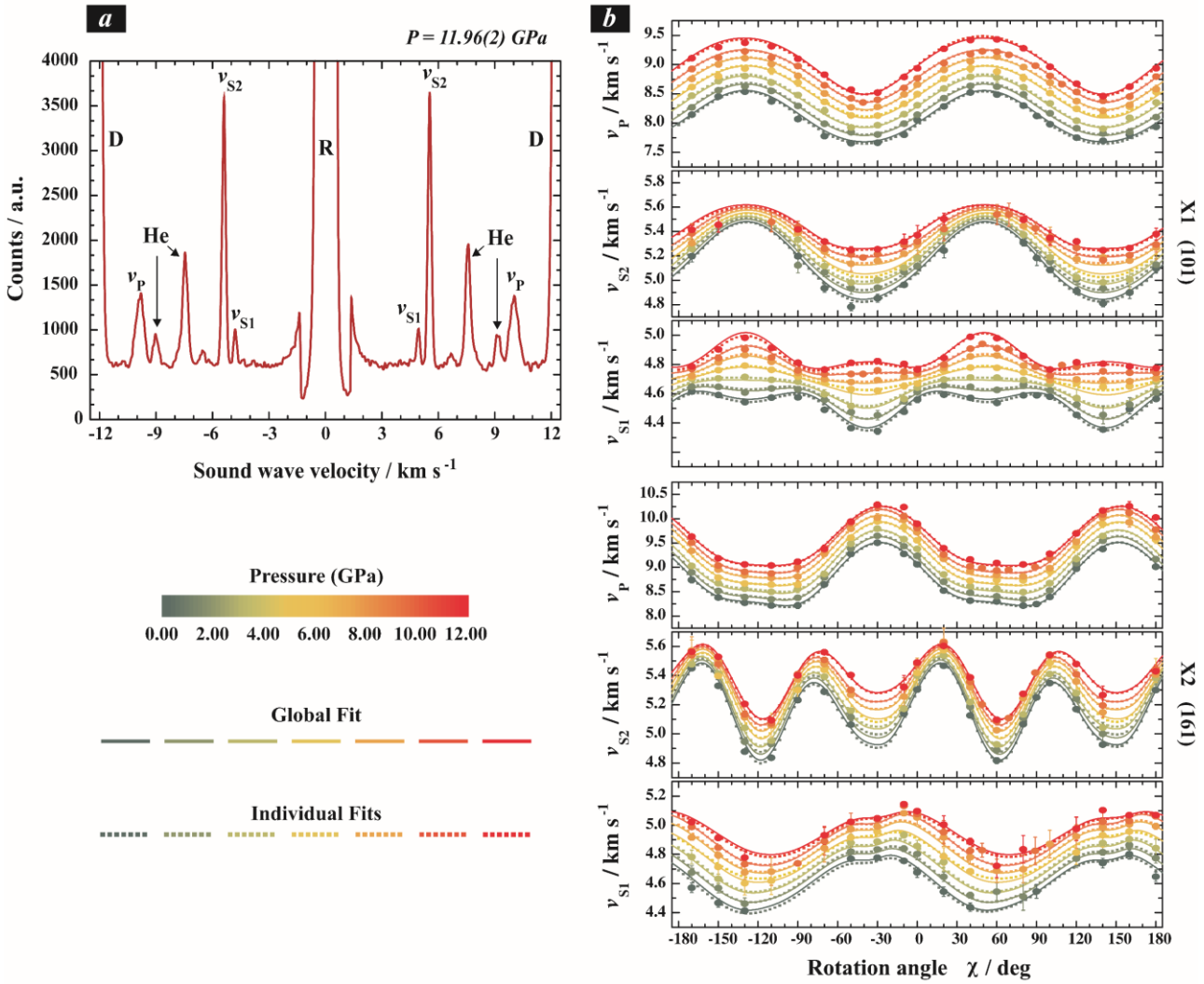


Figure 1. (a) Secondary electron image of a Fo90 olivine platelet oriented parallel to the (161) plane (crystal X2) after the FIB cutting procedure; a superimposed yellow semicircle denotes the sample that was then loaded in the DAC. (b) Cross-polarized light photomicrographs of platelet X2 (161) and X1 (101) inside the sample chamber of the DAC at high pressure, together with a ruby chip (dark black sphere on the left of 101 platelet).



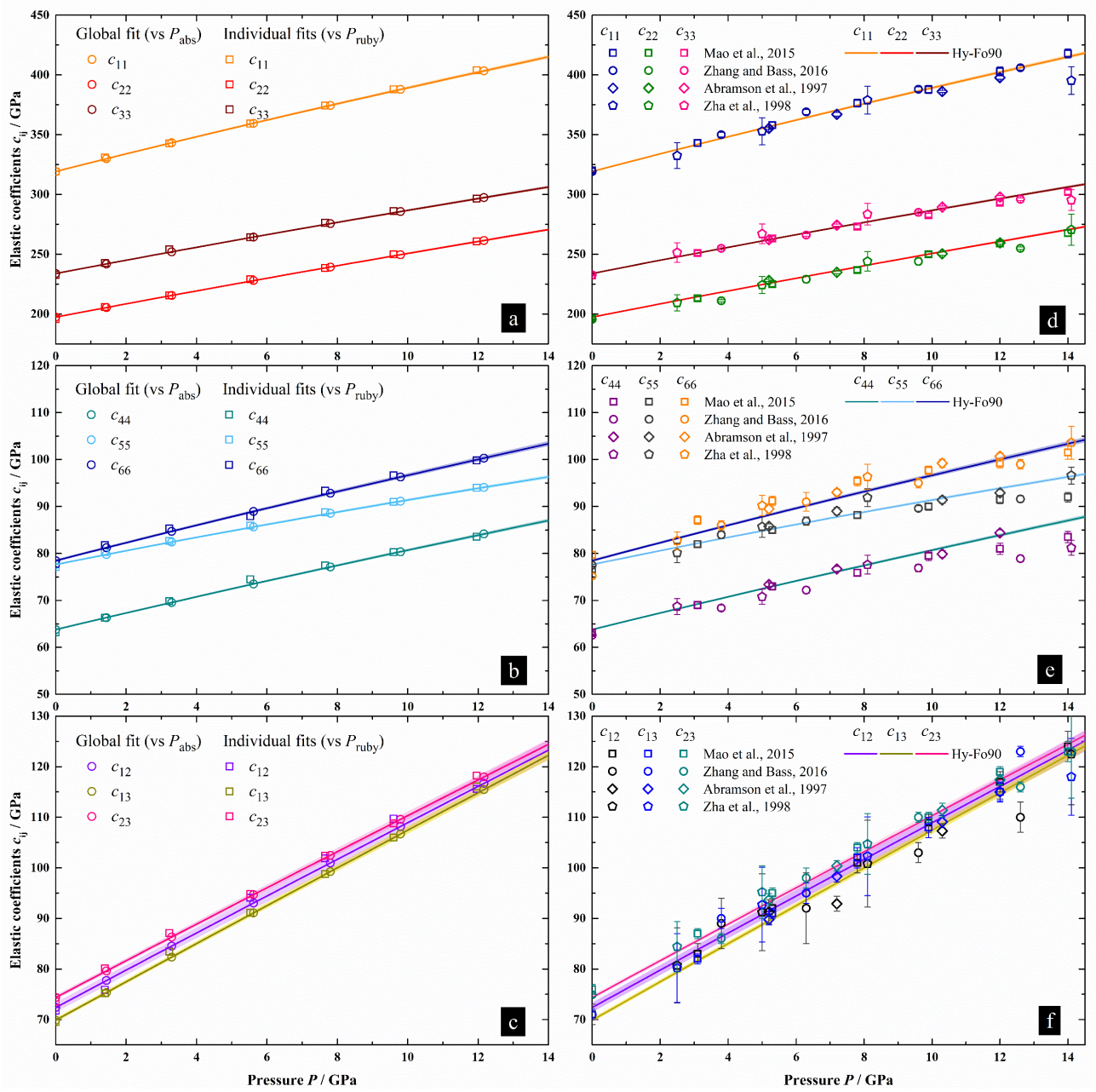
723

724 ***Figure 2.*** Unit-cell parameters and unit-cell volumes (inset) of crystals X1 and X2 normalized with
725 respect to their room pressure values; data were fitted with a third-order Birch-Murnaghan EoS using
726 the EosFit7c program (Angel et al., 2014). Literature data of anhydrous Fo90-92 olivines (Nestola et
727 al., 2011; Zha et al., 1998; Supplementary Table S1) are shown for reference. Note the good
728 agreement between the BM3 fits and relative compression data of hydrous Fo90 olivine and the
729 literature data for the corresponding anhydrous phase.



730

731 ***Figure 3.*** (a) Selected Brillouin spectrum of crystal X2 (161) at 11.96(2) GPa showing distinct and
732 well-resolved compressional v_P, slow and fast shear v_{S1} and v_{S2} wave velocities peaks, as well as
733 spectral contributions of the diamond anvils (D), pressure medium (He) and elastic scattering (R). (b)
734 Data points (filled symbols) as a function of the rotation angle (χ) for both platelets and dispersion
735 curves obtained from the global fit (solid lines) and individual fits (dashed lines), showing excellent
736 agreement between the two fitting strategies.



737

738 ***Figure 4.*** (a-b-c) Comparison of the c_{ij} obtained through the global fit (open circles) and individual
739 fits (open squares), showing values typically identical within two standard deviations (Table 2); the
740 solid lines represent third-order EoS fits of each c_{ij} (global fit parameters) (Table 3). (d-e-f)
741 Comparison of the c_{ij} of anhydrous Fo90 olivines selected from previous literature (Abramson et al.,
742 1997; Mao et al., 2015; Zha et al., 1998; Zhang and Bass, 2016; Supplementary Table S2), and the
743 fits of each c_{ij} (global fit parameters) of hydrous Fo90 olivine obtained in this study. Note that the fits
744 of the experimentally determined c_{ij}s for hydrous olivine and the c_{ij}s of the corresponding anhydrous
745 phase are nearly identical.

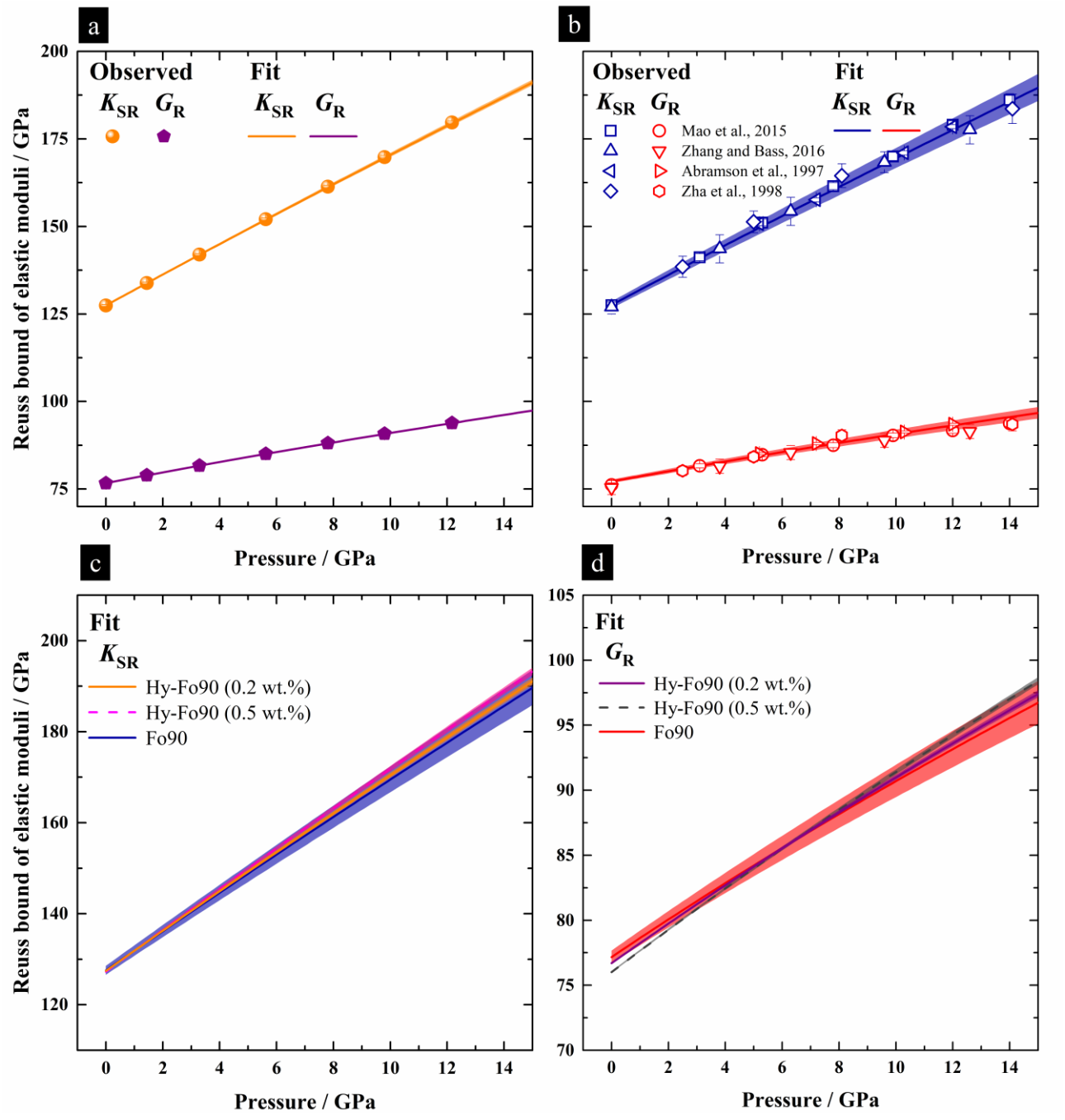


Figure 5. (a) Variation as a function of pressure of the bulk (*K*) and shear (*G*) moduli of hydrous Fo90 calculated in the Reuss bound from the experimental high-pressure elasticity measurements of this study; the solid line and shaded area are the fit of the experimental data and the associated uncertainty, respectively. (b) Variation as a function of pressure of the bulk (*K*) and shear (*G*) moduli of anhydrous Fo90 calculated in the Reuss bound from previous experimental high-pressure elasticity measurements (Abramson et al., 1997; Mao et al., 2015; Zha et al., 1998; Zhang and Bass, 2016; Supplementary Table S2); the solid line and shaded area are the fit of the experimental data and the

754 associated uncertainty, respectively. (c-d) Superimposition of fit curves for hydrous Fo90 and
755 anhydrous Fo90 olivine; the dashed lines represent a linear extrapolation of the effect of incorporation
756 of 0.5 wt. % H2O on the elastic properties of Fo90 olivine (see text and Table 4). Uncertainties are
757 calculated by propagating the experimental errors on density and elastic moduli.

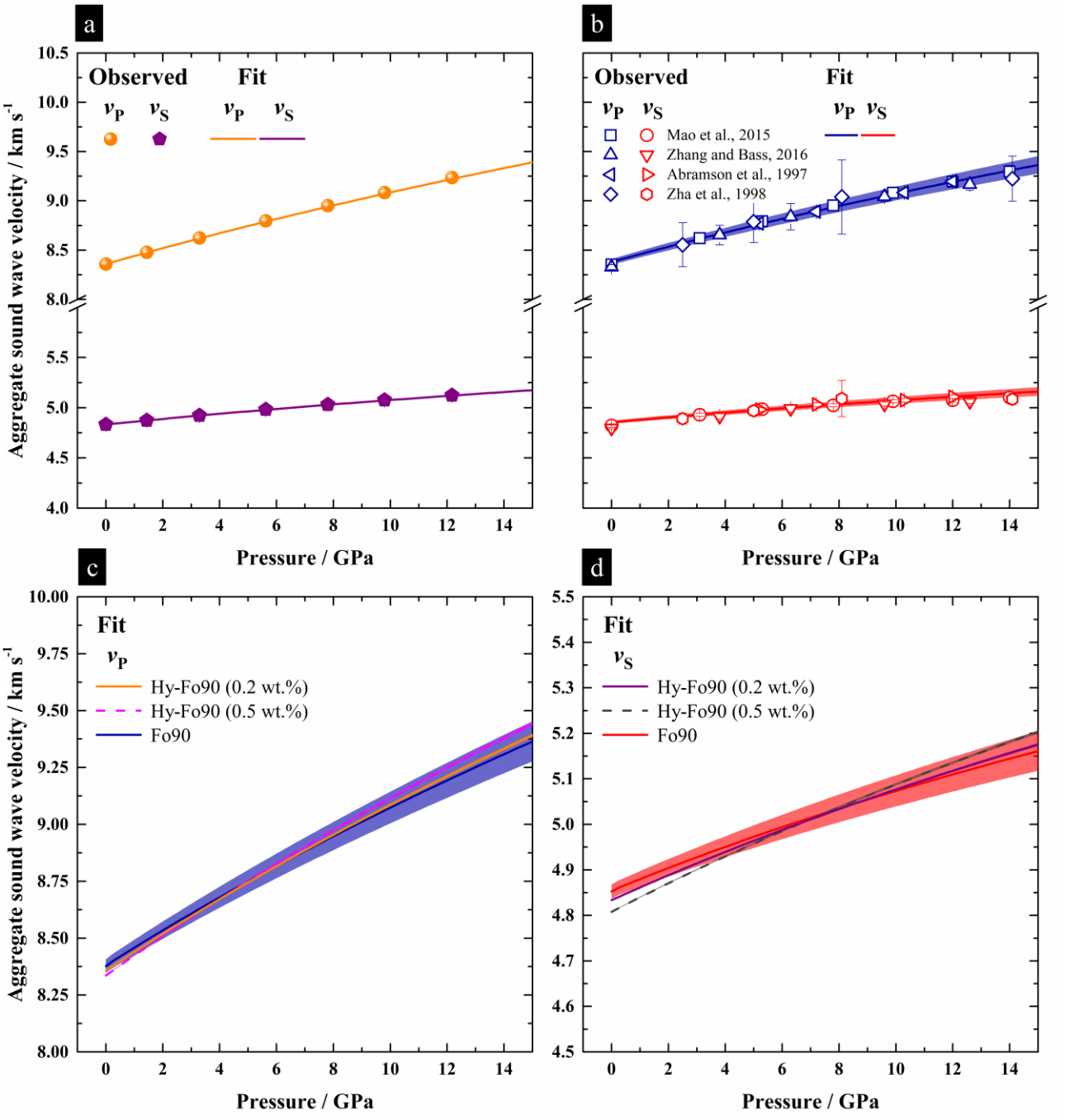


Figure 6. (a) Variation as a function of pressure of the aggregate compressional and shear wave velocities of hydrous Fo90 calculated from the experimental high-pressure elasticity measurements of this study; the solid line and shaded area the fit of the experimental data and the associated uncertainty, respectively. (b) Variation as a function of pressure of the aggregate compressional and shear wave velocities of anhydrous Fo90 calculated from previous experimental high-pressure elasticity measurements (Abramson et al., 1997; Mao et al., 2015; Zha et al., 1998; Zhang and Bass, 2016; Supplementary Table S2); the solid line and shaded area the fit of the experimental data and

766 the associated uncertainty, respectively. (c-d) Superimposition of fit curves for hydrous Fo90 and
767 anhydrous Fo90 olivine. Uncertainties are calculated by propagating the experimental errors on
768 density and elastic moduli.

Tables

Table 1. Unit–cell lattice parameters and volumes of hydrous Fo90 olivine crystals X1 and X2 measured in the DAC experiment. Pressure is calculated using the ruby fluorescence calibration of Shen et al. (2020).

	X1 (platelet *1 0 1*)				X2 (platelet *1 6 1*)			
P (GPa)	**a (Å)**	**b (Å)**	**c (Å)**	**V (Å^3)**	**a (Å)**	**b (Å)**	**c (Å)**	**V (Å^3)**
0.00010(1)	4.7613(5)	10.2243(2)	5.9925(3)	291.72(3)	4.7610(1)	10.2227(3)	5.9921(1)	291.63(1)
1.40(2)	4.7499(7)	10.1753(3)	5.9701(5)	288.55(4)	4.7487(3)	10.1744(5)	5.9700(3)	288.44(2)
3.23(2)	4.7351(5)	10.1147(3)	5.9432(4)	284.64(3)	4.7342(2)	10.1128(4)	5.9423(2)	284.49(2)
5.53(4)	4.7178(7)	10.0455(3)	5.9116(5)	280.16(3)	4.7176(2)	10.0436(4)	5.9108(2)	280.06(2)
7.66(2)	4.7029(6)	9.9847(3)	5.8837(4)	276.28(3)	4.7028(3)	9.9824(7)	5.8826(3)	276.16(3)
9.60(4)	4.6902(7)	9.9313(3)	5.8592(6)	272.92(3)	4.6899(3)	9.9292(5)	5.8581(2)	272.80(2)
11.96(2)	4.6765(6)	9.8731(2)	5.8319(5)	269.27(3)	4.6762(2)	9.8707(4)	5.8309(1)	269.14(1)

Table 2. Elastic stiffness coefficients (c_{ij}) and elastic moduli obtained from the individual fit and global fit procedure, reported in GPa. Numbers in brackets represent one standard deviation (std). ρ uncertainties propagate both the std's of the unit–cell volumes from SCXRD and the chemical composition from EPMA.

Individual Fits

P (GPa)	ρ (g cm^{-3})	c_{11}	c_{22}	c_{33}	c_{44}	c_{55}	c_{66}	c_{12}	c_{13}	c_{23}	K_{SV}	G_V	K_{SR}	G_R	$K_{S\ VHR}$	G_{VHR}
0.00010(1)	3.345(6)	319.2(1.0)	195.7(6)	232.7(7)	63.2(2)	77.1(3)	77.8(3)	71.7(1.2)	69.6(5)	73.5(6)	130.8(4)	79.2(1)	126.5(4)	76.2(1)	128.7(4)	77.7(1)
1.40(2)	3.382(6)	330.8(6)	205.8(4)	242.5(5)	66.3(2)	80.3(2)	81.8(3)	75.9(1.1)	75.2(6)	80.1(4)	137.9(4)	82.2(1)	133.8(4)	79.3(1)	135.9(4)	80.7(1)
3.23(2)	3.428(6)	342.8(6)	215.6(4)	254.0(5)	69.8(3)	82.7(2)	85.3(3)	83.4(9)	83.4(4)	87.1(4)	146.7(3)	84.8(1)	142.4(3)	82.0(1)	144.5(3)	83.4(1)
5.53(4)	3.483(6)	359.2(1.1)	229.1(4)	264.1(6)	74.5(2)	85.9(5)	87.9(5)	94.1(1.8)	91.1(7)	94.8(6)	156.9(5)	87.8(2)	152.5(5)	85.2(1)	154.7(5)	86.5(1)
7.66(2)	3.532(6)	374.3(1.1)	238.6(4)	276.2(8)	77.4(2)	88.7(2)	93.3(3)	101.9(1.4)	98.7(7)	102.3(6)	166.1(4)	91.0(1)	161.3(4)	88.2(1)	163.7(4)	89.6(1)
9.60(4)	3.575(6)	388.1(1.2)	249.8(6)	286.2(9)	80.2(2)	91.0(3)	96.7(3)	109.7(1.8)	106.0(7)	108.8(8)	174.8(5)	93.5(1)	169.8(5)	90.9(1)	172.3(4)	92.2(1)
11.96(2)	3.624(6)	404.0(1.3)	260.7(8)	296.5(9)	83.6(3)	94.0(3)	99.8(4)	115.6(1.6)	116.1(7)	118.2(8)	184.6(5)	96.2(1)	179.4(5)	93.5(1)	182.0(5)	94.8(1)
Global Fit																
0.00010(1)	3.345(6)	319.2(7)	197.4(4)	233.9(5)	63.8(2)	77.6(2)	78.5(3)	72.4(1.0)	69.9(4)	74.3(4)	131.5(3)	79.6(1)	127.4(3)	76.6(1)	129.5(3)	78.1(1)
1.440(7)	3.382(6)	329.9(7)	205.4(4)	241.9(5)	66.3(2)	79.8(2)	81.2(3)	77.7(1.0)	75.3(4)	79.6(4)	138.1(3)	81.8(1)	133.8(3)	78.9(1)	135.9(3)	80.3(1)
3.29(2)	3.428(6)	343.2(8)	215.5(5)	252.0(6)	69.6(2)	82.4(2)	84.7(3)	84.5(1.0)	82.3(5)	86.3(5)	146.3(3)	84.5(1)	142.0(3)	81.7(1)	144.2(3)	83.1(1)
5.62(3)	3.483(6)	359.6(9)	227.9(5)	264.3(7)	73.5(2)	85.6(2)	88.9(3)	93.0(1.2)	91.1(5)	94.7(6)	156.6(4)	87.8(1)	152.1(4)	85.1(1)	154.3(4)	86.4(1)
7.80(4)	3.532(6)	374.5(1.1)	239.3(6)	275.6(8)	77.1(3)	88.6(3)	92.8(4)	101.0(1.4)	99.2(6)	102.5(6)	166.1(4)	90.8(1)	161.4(4)	88.1(1)	163.7(4)	89.5(1)
9.80(5)	3.575(6)	387.9(1.2)	249.6(7)	285.6(9)	80.4(3)	91.1(3)	96.3(4)	108.2(1.6)	106.7(7)	109.6(7)	174.7(5)	93.5(1)	169.8(5)	90.8(1)	172.2(5)	92.1(1)
12.17(7)	3.624(6)	403.4(1.4)	261.5(9)	297.3(1.0)	84.2(4)	94.1(4)	100.3(5)	116.7(1.8)	115.5(8)	118.0(9)	184.7(6)	96.5(2)	179.7(5)	93.8(1)	182.2(5)	95.2(1)

Table 3. Resulting fit parameters of the third-order finite strain expression for the c_{ij} and c_{ij}' for hydrous Fo90 (as shown in Figure 4) and anhydrous Fo90 (Supplementary Figure S2).

	Hydrous Fo90 olivine		***Anhydrous Fo90 olivine***	
	c_{ij}	c'_{ij}	c_{ij}	c'_{ij}
c_{11}	319.2(7)	7.18(9)	320.0(9)	6.65(12)
c_{22}	197.4(4)	5.41(5)	195.9(9)	5.17(11)
c_{33}	233.9(5)	5.43(7)	233.2(6)	5.35(8)
c_{44}	63.8(2)	1.72(2)	63.2(4)	1.61(5)
c_{55}	77.6(2)	1.45(2)	77.7(3)	1.34(5)
c_{66}	78.5(3)	1.87(3)	78.0(6)	1.93(7)
c_{12}	72.4(1.0)	3.57(12)	71.3(1.1)	3.40(14)
c_{13}	69.9(4)	3.67(5)	71.0(7)	3.74(10)
c_{23}	74.3(4)	3.52(6)	75.4(7)	3.39(9)

780 ***Table 4.*** EoS parameters for *K* and *G* in the Voigt and Reuss bound for hydrous and anhydrous Fo90 olivine and $\Delta_{H2O}M$ ([*M*]/wt.% H_2O) values calculated

781 for hydrous Fo90 olivine and hydrous Fo100 forsterite.

Anhydrous Fo90 olivine – best fit

	K_{SV}	G_V	K_{SR}	G_R
M_0 **(GPa)**	131.8(1.0)	80.2(5)	127.5(1.0)	77.2(5)
M'_0	4.29(14)	1.42(5)	4.33(14)	1.48(6)

This study – Hydrous Fo90 olivine (global fit parameters)

	K_{SV}	*Effect of* H_2O *(%)*	G_V	*Effect of* H_2O *(%)*	K_{SR}	*Effect of* H_2O *(%)*	G_R	*Effect of* H_2O *(%)*
M_0 **(GPa)**	131.5(2)	–0.2	79.57(6)	–0.7	127.4(2)	–0.1	76.70(6)	–0.6
M'_0	4.40(3)	2.5	1.49(1)	5.2	4.44(3)	2.6	1.55(1)	4.9

$\Delta_{H_2O}M([M]/wt.\%\ H_2O)^1$ ***– Hydrous Fo90 olivine***

	K_{SV}	G_V	K_{SR}	G_R
M_0 **(GPa)**	–1.5(5.1)	–3.2(2.6)	–0.5(5.1)	–2.5(2.5)
M'_0	0.55(0.72)	0.35(0.26)	0.55(0.72)	0.35(0.31)

$\Delta_{H_2O}M([M]/wt.\%\ H_2O)^1$ ***– Hydrous Fo100 forsterite [data from Mao et al., 2010 and Zha et al., 1996]***

	K_{SV}	G_V	K_{SR}	G_R
M_0 **(GPa)**	–4.0(0.8)	–2.7(0.4)	–2.8(0.7)	–2.6(0.4)
M'_0 [2]	0.33(0.23)	0.39(0.13)	0.33(0.23)	0.39(0.13)

Hydrous Fo90 olivine – extrapolation to 0.5 wt.% H_2O

	K_{SV}	*Effect of* H_2O *(%)*	G_V	*Effect of* H_2O *(%)*	K_{SR}	*Effect of* H_2O *(%)*	G_R	*Effect of* H_2O *(%)*
M_0 **(GPa)**	131.1(2)	–0.5	78.60(6)	–2.0	127.3(2)	–0.2	76.00(6)	–1.5
M'_0	4.56(3)	6.4	1.60(1)	13.0	4.61(3)	6.4	1.66(1)	12.4

782 [1] Δ_{H2O}M values yield the change in *K*, *G*, K', and G' for a reference water content of 1 wt.%.
783 [2] We assumed that M'_0 in the Voigt-Reuss-Hill bound ≈ M'_0 in the Voigt and Reuss bounds.